To be published in SPIE Microlithography '97, 3048-24

Characterization of an EUV Schwarzschild objective using phase-shifting point diffraction interferometry

Kenneth A. Goldberg[a,b], Edita Tejnil[a,c], Sang Hun Lee[a,c], Hector Medecki[a], David T. Attwood[a,c], Keith H. Jackson[a], Jeffrey Bokor[a,c]

[a]Center for X-Ray Optics, Lawrence Berkeley National Laboratory, Berkeley, CA 94720
[b]Physics Department, University of California, Berkeley, CA 94720
[c]EECS Department, University of California, Berkeley, CA 94720

ABSTRACT

We report wavefront measurement of a multilayer-coated, reflective optical system at 13.4-nm wavelength performed using a novel phase-shifting point-diffraction interferometer. Successful interferometric measurements of a 10x Schwarzschild objective designed for extreme ultraviolet projection lithography with 0.1-µm resolution demonstrate high-precision with sub-nanometer resolution. The goal of the interferometry is to achieve wavefront measurement accuracy beyond λ/50 rms at EUV wavelengths. Preliminary measurements are discussed and the paths toward achieving the target accuracy are identified.

Keywords: interferometry, point-diffraction interferometry, phase-shifting interferometry, extreme ultraviolet lithography

1. INTRODUCTION

To achieve 0.1-micron critical dimension pattern transfer with extreme ultraviolet (EUV) projection lithography at 13.4-nm wavelength, nearly diffraction-limited, multilayer-coated, reflective optical systems with 0.1 numerical aperture are required.[1] A suggested wavefront aberration tolerance of 0.02 waves rms, or 0.27 nm, places high demands not only on the fabrication of EUV optics and multilayer coatings, but also on the metrology required to characterize these optical systems.[2] The EUV wavefront is determined by the geometrical figure of the mirror surfaces and by the properties of the multilayer coatings, which are deposited with graded layer thickness across mirror areas of several square centimeters. Optical aberrations arising from multilayer coating defects and thickness errors are measurable only at the EUV operational wavelength of the system. Furthermore, the final alignment and qualification of an optical system must be performed at-wavelength. These factors motivate the development of highly-accurate, EUV, wavefront-measuring interferometry.

Implementation and development of a phase-shifting point diffraction interferometer (PS/PDI)[3] at EUV wavelengths is now in progress on an undulator beamline at Lawrence Berkeley Laboratory's Advanced Light Source synchrotron radiation facility.[4,5] The EUV PS/PDI system is used to perform interferometric measurements of a multilayer-coated Schwarzschild objective, designed to operate with 10x demagnification and 0.1 µm-resolution at 13.4-nm wavelength in a prototype EUV projection lithography system.[6]

Concurrent with the development of EUV interferometry, the capability to perform high-accuracy PS/PDI measurements with visible light in the same experimental system is being developed. Direct comparison of EUV and visible-light measurements of an optical system may reveal important characteristics in the behavior of multilayer coated optics.

This paper describes recent results from experiments in progress, including EUV and visible-light measurements. The first EUV PS/PDI measurements demonstrate the high degree of precision possible with this technique.

2. PS/PDI DESCRIPTION

The PS/PDI is a type of point diffraction interferometer, modified for improved efficiency and phase-shifting capability. It enables direct measurement of a spatially coherent wavefront propagated through an optical system under test. With its relaxed coherence length requirements and relatively simple design, the PS/PDI is well-suited to measurement of nearly diffraction-limited optical systems over a broad range of wavelengths.

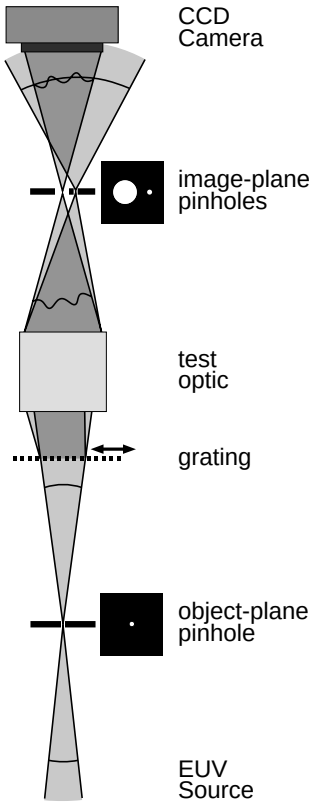

Figure 1. Key elements of the PS/PDI.

Figure 1 shows a schematic representation of the EUV PS/PDI. The optical system under test is coherently illuminated by light diffracted from an object-plane pinhole spatial filter, or *object pinhole.* A coarse transmission grating, placed between the object pinhole and the test optic, serves as a beam-splitter, diffracting multiple overlapping beams corresponding to the orders of the grating diffraction. Those beams which are diffracted at sufficiently low angles to enter the aperture of the test optic propagate through the optical system and form a series of displaced foci in the image plane.

Two adjacent beams are selected to become the interferometer's *test* and the *reference* beams, respectively; all other beams are blocked by an opaque membrane in the image plane. The central beam, which originates from the transmitted, zero-th grating order, is chosen to be the test beam. This beam contains the aberrations in the optical system and is allowed to pass unattenuated, through a window in the opaque image-plane membrane. Near this window, a small, sub-resolution *reference pinhole* is placed at the focus of one of the first-order beams. Light diffracted from this pinhole produces a displaced, spherical, diverging reference beam that interferes with the test beam across the numerical aperture of interest. Any aberrations in the reference, which are introduced by the test optic, or the grating beam-splitter, are removed by the reference pinhole spatial filter.

The resultant interference fringe pattern reveals the optical path difference (OPD) between the test and reference beams. The fringes represent contours of constant path difference, separated by one wavelength. To the extent that the reference pinhole diffracts a perfect, spherical reference wave, measurement of the OPD reveals the aberrations in the test beam.

The test beam is transmitted through the grating; its phase is therefore not affected by the grating position. The reference beam, however, is generated by diffraction from the grating rulings. Hence lateral translation of the grating in the direction normal to the grating rulings produces a periodic phase-shift in the diffracted reference beam. In this way, control of the grating position enables the introduction of the variable phase-shift between the test and reference beams necessary for phase-shifting interferometry.

The spatial resolution of PS/PDI is determined by the resolution of the detector array and by the size of the image plane window, through which the test beam passes. By transmitting only the region surrounding the test-beam focus, the window acts as a low-pass filter in the spatial-frequency domain. The relevant length scale in the image plane is λ/NA, which is approximately equal to twice the diffraction limited resolution of the optic. The shape and size of the window (typically 20-40 times λ/NA wide) determines the spatial frequencies transmitted. Depending on the image-plane separation of the grating orders, and on the point-spread function of the test optic, the test beam will overlap the other beams to some extent. This overlap, in the region of the window, adds spurious high-spatial-frequency errors to the measurement. Therefore, the maximum allowable size of the window is limited by the separation of the test and reference beams necessary to prevent overlap. In the direction perpendicular to the beam separations, however, the limitations are relaxed, and the window may be enlarged to increase the high-frequency response in that direction. In principle, a set of two measurements recorded with 90° rotation of the fringe pattern (grating orientation) may be used to reconstruct higher-frequency aberration content along both directions.

3. EXPERIMENTAL CONFIGURATION OF THE PS/PDI

The experimental configuration of the PS/PDI is shown in Fig. 2. The 10x Schwarzschild objective test optic contains two, nearly concentric, spherical mirrors: a convex primary and an annular, concave secondary. The optic is designed to have a vertically oriented optic axis, with object-plane illumination coming from below. A removable aperture stop rests against the primary mirror and defines an unobstructed, off-axis, circular sub-aperture corresponding to an object-side numerical aperture (NA) of 0.008, inclined 1.2° from the vertical. With a demagnification of 10:1, the image-side NA is 0.08. Three balls mounted at the top of the optic housing define the image plane and central field point, determined during the assembly of the optic. In the image plane, the optic has a circular field of view, 400 µm in diameter, and a 1-µm depth of focus.[6]

3.1 Configuration for EUV interferometry

An undulator beamline, containing a grating monochromator followed by a Kirkpatrick-Baez mirror pair (K-B), delivers radiation from the undulator to the interferometer.[7,8] The angular demagnification of the beamline is designed to maximize the coherent flux available for illumination of the Schwarzschild objective. The entire system operates under vacuum, in pressures ranging from 10^{-9} torr in the beamline to 10^{-6} torr in the interferometer chamber.

In conjunction with the undulator, the monochromator allows the wavelength to be tuned continuously from 5 to 25 nm, with a spectral resolution in the range of $\lambda/\Delta\lambda \sim 200\text{-}1000$. To achieve good fringe contrast, the interferometer requires a source coherence length greater than the largest path-length difference encountered in the interferometer. In a system designed for approximately 50 fringes across the aperture, this requirement translates into a spectral resolution of $\lambda/\Delta\lambda$ greater than 50. The resolution of the monochromator is therefore sufficient for this experiment, as demonstrated experimentally by observed EUV interferogram fringe contrasts of 90%.

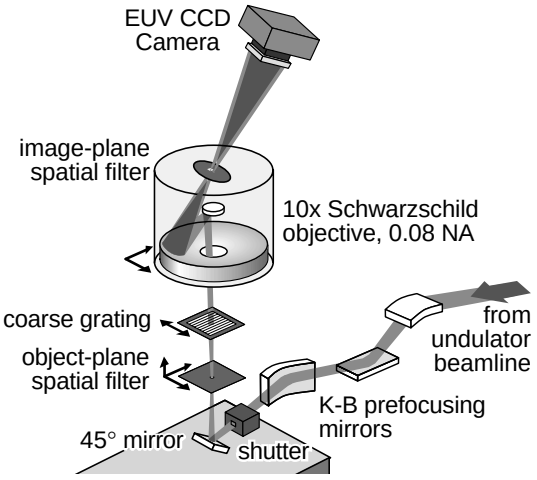

Figure 2. Arrangement of optical elements for EUV PS/PSI measurement of the 10x Schwarzschild objective.

To illuminate the Schwarzschild objective vertically, a flat, multilayer-coated turning mirror, mounted at an angle of incidence near 45 degrees, is placed between the K-B and its focus, directing the beam upward. The angle and longitudinal position of this turning mirror are adjustable to enable alignment and the investigation of wavefront aberrations across the field of view of the optic. A high-speed shutter, placed between the K-B mirrors and the flat turning mirror, controls the exposure time of the measurements and also protects the optical system from EUV exposure when the beam is not being used.

In the focal plane of the K-B, coincident with the object plane of the test optic, the sub-micron object pinhole is held in a kinematic mount attached to a three-axis stage. The stage enables horizontal translation of the object pinhole to position it within the narrow beam and vertical translation to bring the pinhole into the desired object plane.

A coarse grating beam-splitter is placed between the object pinhole and the entrance aperture of the test optic. The grating, typically 18-40 µm pitch, is made of a gold absorber pattern on a 1000-Å thick silicon-nitride membrane, with 0.5 x 0.5 cm^2 area. The grating is held on a one-dimensional horizontal translation stage, with motion in the direction perpendicular to the rulings, to enable phase-shifting. This fine, 0.1-µm resolution grating stage is attached to a coarse translation mechanism that allows the grating to be retracted completely from the beam.

With the beam and object pinhole held stationary, alignment of the image point within the image plane is performed by a two-axis lateral translation of the test optic. This translation with respect to a stationary object point takes advantage of the 10x demagnification to enable positioning of the image point with better than 0.1-µm resolution.

The PS/PDI pinhole pairs used in the EUV experiments are made of a patterned gold absorber layer on a solid silicon-nitride membrane, fabricated by electron beam lithography. The pairs consist of a sub-100-nm reference pinhole adjacent to a square window, 5.0 µm on edge, with a center-to-center separation of 4.5 µm. A kinematic mount, which rests on the three balls that define the image plane, holds the pinholes inclined at 12 degrees, normal to the central ray of the off-axis beam. The pinholes are manually pre-aligned within the mount and remain stationary with respect to the test optic. Typically, the image plane contains a square array of pinhole pairs, separated by 40 µm, facilitating the study of several field points.

Data is recorded with a back-thinned, back-illuminated, un-coated, 1024 x 1024 pixel, 1-square-inch area, 16-bit Tektronix CCD camera optimized for EUV detection. The CCD, also mounted at angle of 12-degrees from the vertical to receive the central ray at normal incidence, occupies a plane 12 cm beyond the image plane.

3.2 Modification for visible-light interferometry

In addition to EUV interferometric measurements, visible-light interferometry can also be performed with only minimal modification of the system. The key component is a special flange, depicted in Fig. 3, that serves as a kinematic mount attached to a 3-axis translation stage for positioning of the object point. The visible beam from a 5-mW helium-neon laser is introduced into the vacuum chamber via an optical fiber that delivers spatially coherent illumination from its polished tip. The fiber enters the system horizontally, at the position of the object pinhole holder. Light diffracted from the tip of the fiber is reflected upward by a small, flat, mirror mounted at 45 degrees. The region of the mirror used to reflect the beam is very small and is sufficiently flat to avoid introducing aberrations into the illuminating beam. A shutter outside of the vacuum chamber, located between the laser and the input end of the fiber, controls the exposure time of the measurements.

The same coarse gratings are used in both the visible-light and the EUV measurements to achieve the same fringe density in the measured interferograms. However, the diffraction angle separating the test and reference beams, and the separation distance between the beams in the image plane, scale linearly with the wavelength. To ensure that the reference beam will reach the entrance pupil of the test optic, a coarser-pitch grating may be necessary for visible-light measurements.

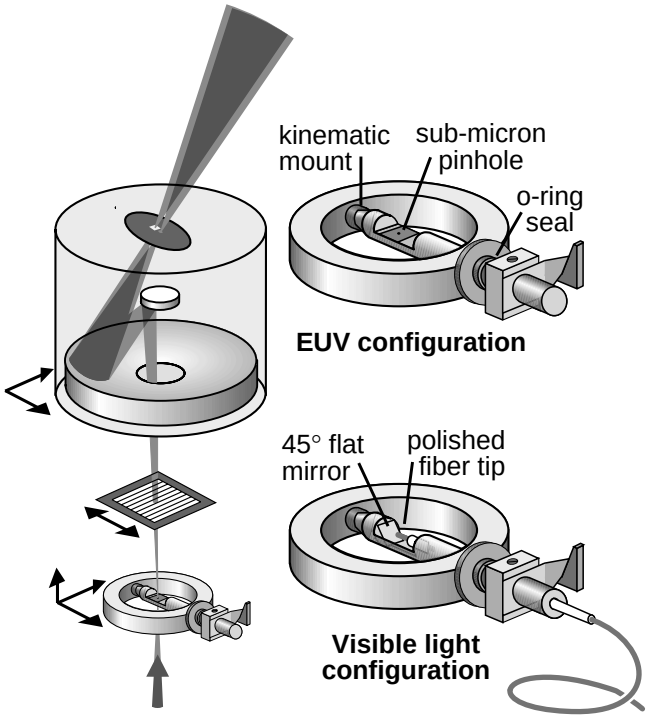

Figure 3. Illustration of the special flange that enables easy conversion between EUV and visible light illumination. EUV light from the undulator beamline is filtered by a sub-micron object pinhole. Visible light may be introduced into the chamber via an optical fiber with a polished tip. This flange holds the source in a kinematic mount attached to a three-axis stage.

4. ANALYSIS OF INTERFEROMETRIC MEASUREMENTS

The first EUV PS/PDI measurements of the 10x Schwarzschild objective were performed in December, 1996. These are the first such measurements of a multilayer-coated, reflective, EUV optical system. They demonstrate, that the necessary alignment, positioning, and stability requirements have been achieved, and that the EUV source has sufficient flux and longitudinal coherence to enable repeatable wavefront measurements with a high-degree of precision.

Figure 4 is one interferogram from a series of measurements discussed here. The fringes show the interference of the test beam from the optical system, and the displaced, spherical reference beam generated by diffraction from the reference pinhole.

Once beam alignment and coarse positioning have been performed, the interference fringes can be attained quite readily. With real-time feedback from the CCD detector, horizontal positioning of the optic and vertical positioning of the object pinhole bring the test and reference beams

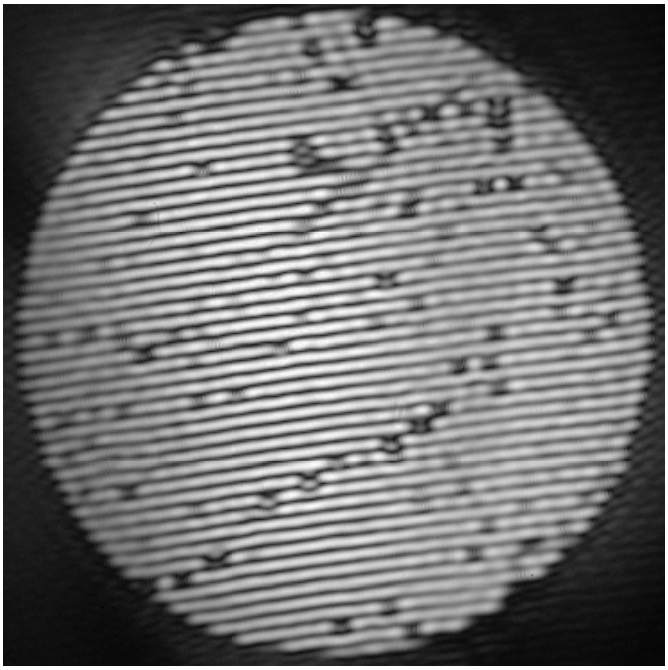

Figure 4. An EUV PS/PDI interferogram of the 10x Schwarzschild objective test optic.

into the vicinity of the image-plane window. Fine adjustments then place the reference pinhole into the focus of the reference beam, and the interference fringes appear. The measured fringe patterns are stable and repeatable, and demonstrate good fringe visibility across the entire aperture.

4.1 Determination of the wavefront phase

A typical EUV interferogram is shown in Figs. 4 and 5c. Analysis reveals a wavefront that represents the aberrations in the optical system, plus the additive contributions of systematic error sources, not yet fully characterized.

Analysis of the data with phase-shifting interferometry was impaired by a carbon contamination problem, discussed in Section 4.2. Therefore, to retrieve the OPD from the interferograms, a Fourier-transform method of fringe pattern analysis,[9,10] employing a Gaussian filter in the spatial-frequency domain, was applied separately to three recorded interferograms. These measurements were originally part of a phase-shifting series, with a quarter-cycle phase-shift between each. The region of data under consideration has a circular area, 690 pixels in diameter, with approximately 3.7×10^5 individual points. After phase-unwrapping[11] and removal of the arbitrary average phase offset from each image, a single composite surface was formed from the point-by-point average of the three measurements. Finally, the wavefront was fit to a set of the first 37 Zernike polynomials,[12,13] and the *tilt* and *defocus* components were removed. The wavefront phase map is shown in Fig. 5d.

To reduce spurious contributions from the numerous dark regions in the data (discussed in Section 4.2), the wavefront was reconstructed from a series of the first 37 Zernike polynomials, excluding the measurement-dependent tilt and defocus terms. The reconstruction has an RMS wavefront error of 0.082 waves, or 1.10 nm, and a peak-to-valley magnitude of 0.530 waves, or 7.10 nm.

The agreement between the three wavefront measurements can be characterized by the mean value of the point-by-point uncertainty. The measurement precision of the raw data is found to be 0.0045 waves, or 0.060 nm. The precision of the data reconstructed from the Zernike polynomials, fit separately to each of the three measurements, is 0.0025 waves, or 0.034 nm, showing that much of the uncertainty comes from the localized dark regions.

Presented here, before the characterization and removal of systematic measurement errors, the nanometer-scale magnitudes of the wavefront aberrations are very significant. They represent an upper bound on both the magnitude of the systematic errors, and on the quality of the test optic.

4.2 Experimental challenges

We are now working to address several significant measurement challenges: possible aberrations in the reference wavefront, carbon contamination of the image-plane membrane, and defects in the test optic.

With an operating vacuum pressure on the order of 10^{-6} torr in the test optic chamber, carbon contamination of the surfaces receiving the highest EUV intensity can be an issue. Most critically, EUV transmission through the image-plane pinhole pair decreases relatively quickly. There is, however, no evidence to suggest that the power incident on the pinhole membrane is

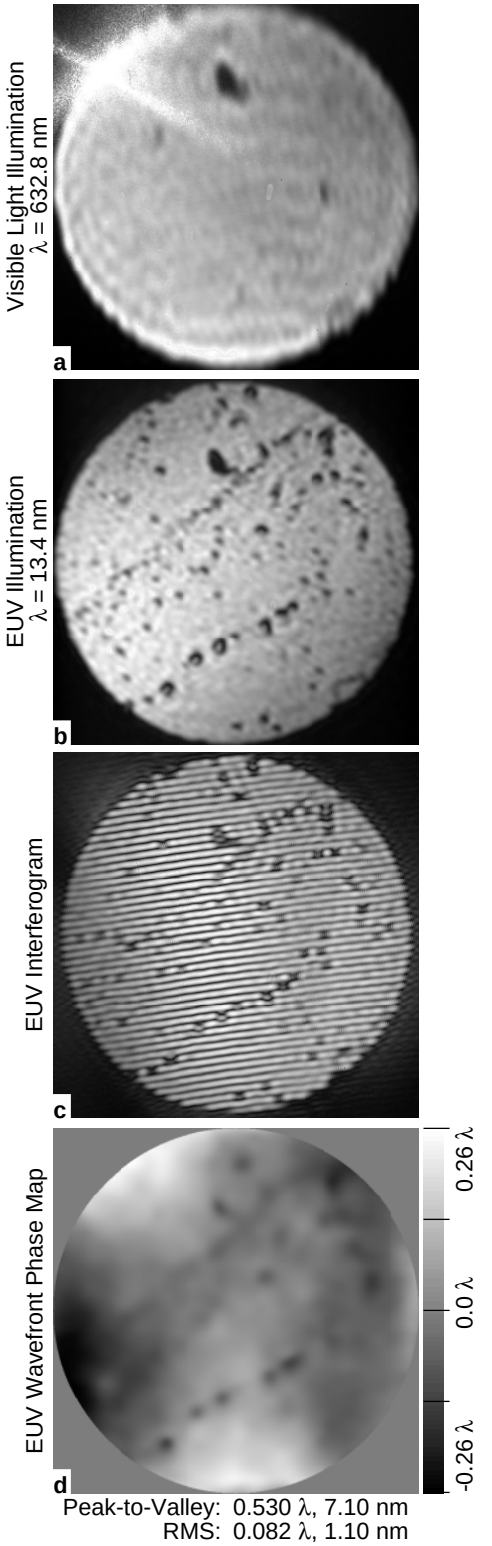

Figure 5. Visible-light **(a)** and EUV **(b)** test-beam transmission through the 10x Schwarzschild objective. **(c)** An EUV interferogram. **(d)** An EUV wavefront phase map calculated from three interferograms. Peak-to-valley and rms wavefront distortion are based on data reconstructed from the Zernike polynomial fit.

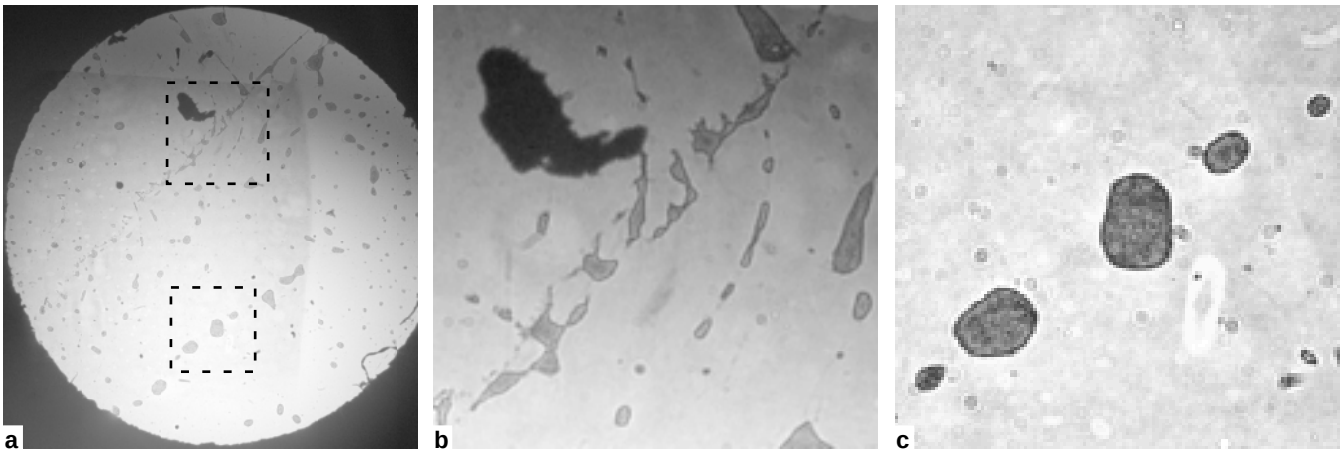

Figure 6. (a) Transmission of a uniform beam through the 10x Schwarzschild objective at 13.4-nm wavelength, recorded 12 cm beyond the image plane. **(b,c)** Enlarged details of the two regions in (a) denoted by dashed rectangles. These dark spots originate from numerous ~100-µm-sized defects in the primary mirror. It is unknown whether some of these defects are on or below the mirror-coating surfaces. The contrast in (b) and (c) has been enhanced to reveal the structure of the defects.

great enough to cause damage due to local heating. The photon flux incident on the reference pinhole is determined by the measured flux through the object pinhole, and the estimated efficiencies of the grating and the Schwarzschild objective, to be on the order of 10^5 W/cm^2 in the region of the 0.1-µm foal spot. Earlier studies have shown that power absorption of this magnitude raises the membrane temperature by less than 1°C.[14]

Phase-shifting interferometry relies on the combination of successive, phase-shifted measurements, recorded under constant experimental conditions. When the experimental conditions change between measurements, phase-shifting analysis is ineffective, and single-image interferogram analysis techniques must be applied.

A second measurement limitation, apparent in Figures 4, 5, and 6, is the presence of numerous defects in the test optic. In addition to tiny particles that are visible by eye on the mirror surfaces, Fig. 6 shows what appears to be the residue left by a wet-cleaning process at some stage of the fabrication. The concave secondary mirror projects a real image of the entrance pupil (which rests on the primary mirror) onto a plane 5 cm before the CCD detector. Sharp features in the illumination pattern can thus be attributed to defects on the primary mirror. The presence of particles and localized reflectance non-uniformities creates low-angle scattered light that increases the overlap of the test and reference beams and corrupts the measurements in the vicinity of these regions by introducing phase discontinuities.

Many of the small defects apparent in the EUV images are not resolvable in the visible light measurements. This can be seen by comparison of Figures 5a and b, which show the transmitted intensities in the visible-light and EUV test beams. In both cases, the test beams pass through an image-plane window (4.5-µm wide for the EUV, and 120-µm wide for the visible light), resulting in the filtration of the highest spatial frequencies.

5. CONCLUSION

High-accuracy wavefront measuring interferometry of extreme ultraviolet optical systems using a novel phase-shifting point diffraction interferometer is under development at the Advanced Light Source. First measurements of a multilayer-coated 10x Schwarzschild objective, designed for EUV lithography experiments at 13.4 nm wavelength, reveal system wavefront aberrations on the order of 1 nm rms, with a measurement precision of 0.06 nm. Characterization of the measurement accuracy is in progress. With only minor modification, the experimental system has the capability for concurrent, visible-light interferometry.

ACKNOWLEDGMENTS

The authors gratefully acknowledge the contributions of Phil Batson, Paul Denham, James Galvin, Drew Kemp, Senajith Rekewa, and Joshua Cantrell for engineering and design support, and Erik Anderson for the fabrication of image-plane pinholes. This research was supported by Intel, SRC, DARPA Defense Advanced Lithography Program, and DOE Office of Basic Energy Sciences.

REFERENCES

1. M. D. Himel, "Optic Fabrication and Metrology for Soft X-Ray Projection Lithography," *OSA Proceedings on Soft X-Ray Projection Lithography*, A. M. Hawryluk, and R. H. Stulen, eds., **18**, pp. 108-9, Optical Society of America, Washington, DC, 1993.
2. D. M. Williamson, "The elusive diffraction limit," *OSA Proceedings on Extreme Ultraviolet Lithography*, F. Zernike, D. T. Attwood, eds., **23**, pp. 68-76, Optical Society of America, 1994,
3. H. Medecki, *et al.*, "A Phase-Shifting Point Diffraction Interferometer," Optics Letters, **21**, 19, pp. 1526-8, 1996
4. E. Tejnil, *et al.*, "Phase-shifting point diffraction interferometry for at-wavelength testing of lithographic optics," *OSA TOPS Volume on Extreme Ultraviolet Interferometry*, 1996.
5. K. A. Goldberg, *et al.*, "Progress toward λ/20 EUV interferometry," Journal of Vacuum Science & Technology B, **13**, 6, pp. 2923-7, 1995.
6. D. A. Tichenor, *et al.*, "Development and characterization of a 10x Schwarzschild system for SXPL," *OSA Proceedings on Soft X-Ray Projection Lithography*, Andrew M. Hawryluk and Richard H. Stulen, eds., **18**, pp. 79-82, 1993.
7. D. Attwood, *et al.*, "Undulator radiation for at-wavelength interferometry of optics for extreme-ultraviolet lithography," Applied Optics, **32**, 34, pp. 7022-7031, 1993.
8. R. Beguiristain, *et al.*, "Characterization of thermal distortion effects on beamline optics for EUV interferometry and soft x-ray microscopy," Rev. Sci. Instrumen. **67**, 9, pp. 1-9, 1996.
9. W. W. Macy, Jr., "Two-dimensional fringe-pattern analysis," Applied Optics, **22**, 23, pp. 3898-3901, 1983.
10. D. J. Bone, *et al.*, "Fringe-pattern analysis using a 2-D Fourier transform," Applied Optics, **25**, 10, pp. 1653-1660, 1986.
11. D. Malacara, ed., *Optical Shop Testing, Second Edition*, Ch. 14, Wiley, New York, 1992.
12. J. Y. Wang, *et al.*, "Wave-front interpretation with Zernike polynomials," Applied Optics, **19**, 9, pp. 1510-18, 1980.
13. D. J. Fisher, *et al.*, "Vector formulation for interferogram surface fitting," Applied Optics, **32**, 25, 4738-43, 1993.
14. K. A. Goldberg, *et al.*, "Point diffraction interferometry at EUV wavelengths," *OSA Proceedings on Extreme Ultraviolet Lithography*, F. Zernike, D. T. Attwood, eds., **23**, pp. 134-41, Optical Society of America, 1994,

Further Author information –

K. A. G.: Email: KAGoldberg@lbl.gov; WWW: http://xray.eecs.berkeley.edu:8080/kgoldberg; Telephone: 510-486-4079; Fax: 510-486-4550

E. T.: Email: tejnil@eecs.berkeley.edu; WWW: http://xray.eecs.berkeley.edu:8080/tejnil

S. H. L.: Email: shlee@grace.lbl.gov; WWW: http://xray.eecs.berkeley.edu:8080/shlee

D. T. A.: Email: DTAttwood@lbl.gov

K. H. J.: Email: KHJackson@lbl.gov

J. B.: Email: jbokor@eecs.berkeley.edu; WWW: http://www.eecs.berkeley.edu/~jbokor